Gas-Phase Conformations and Energetics of Protonated 2'-Deoxyguanosine and Guanosine: IRMPD Action Spectroscopy and Theoretical Studies

ARTICLE *in* THE JOURNAL OF PHYSICAL CHEMISTRY B · NOVEMBER 2014

Impact Factor: 3.3 · DOI: 10.1021/jp508019a · Source: PubMed

5 AUTHORS, INCLUDING:

Ranran Wu
Wayne State University
12 PUBLICATIONS **53** CITATIONS
SEE PROFILE

Bo Yang
Vanderbilt University
16 PUBLICATIONS **102** CITATIONS
SEE PROFILE

Mary T Rodgers
Wayne State University
125 PUBLICATIONS **4,177** CITATIONS
SEE PROFILE

THE JOURNAL OF PHYSICAL CHEMISTRY B

Article

pubs.acs.org/JPCB

Gas-Phase Conformations and Energetics of Protonated 2′-Deoxyguanosine and Guanosine: IRMPD Action Spectroscopy and Theoretical Studies

R. R. Wu,[†] Bo Yang,[†] G. Berden,[‡] J. Oomens,[‡,§] and M. T. Rodgers*[,†]

[†]Department of Chemistry, Wayne State University, Detroit, Michigan 48202, United States

[‡]Institute for Molecules and Materials, Radboud University Nijmegen, FELIX Facility, Toernooiveld 7, 6525 ED, Nijmegen, The Netherlands

[§]van't Hoff Institute for Molecular Sciences, University of Amsterdam, Amsterdam, The Netherlands

Supporting Information

ABSTRACT: The gas-phase structures of protonated 2′-deoxyguanosine, $[dGuo+H]^+$, and its RNA analogue protonated guanosine, $[Guo+H]^+$, are investigated by infrared multiple photon dissociation (IRMPD) action spectroscopy and theoretical electronic structure calculations. IRMPD action spectra are measured over the range extending from ∼550 to 1900 cm^{-1} using the FELIX free electron laser and from ∼2800 to 3800 cm^{-1} using an optical parametric oscillator/amplifier (OPO/OPA) laser system. The measured IRMPD spectra of $[dGuo+H]^+$ and $[Guo+H]^+$ are compared to each other and to B3LYP/6-311+G(d,p) linear IR spectra predicted for the stable low-energy conformations computed for these species to determine the most favorable site of protonation, identify the structures accessed in the experiments, and elucidate the influence of the 2′-hydroxyl substituent on the structures and the IRMPD spectral features. Theoretical energetics and the measured IRMPD spectra find that N7 protonation is preferred for both $[dGuo+H]^+$ and $[Guo+H]^+$, whereas O6 and N3 protonated conformers are found to be much less stable. The 2′-hydroxyl substituent does not exert a significant influence on the structures and relative stabilities of the stable low-energy conformations of $[dGuo+H]^+$ versus $[Guo+H]^+$ but does provide additional opportunities for hydrogen bonding such that more low-energy structures are found for $[Guo+H]^+$. $[dGuo+H]^+$ and $[Guo+H]^+$ share very parallel IRMPD spectral features in the FELIX and OPO regions, whereas the effect of the 2′-hydroxyl substituent is primarily seen in the relative intensities of the measured IR bands. The measured OPO/OPA spectral signatures, primarily reflecting the IR features associated with the O−H and N−H stretches, provide complementary information to that of the FELIX region and enable the conformers that arise from different protonation sites to be more readily distinguished. Insight gained from this and parallel studies of other DNA and RNA nucleosides and nucleotides should help better elucidate the effects of the local environment on the overall structures of DNA and RNA.

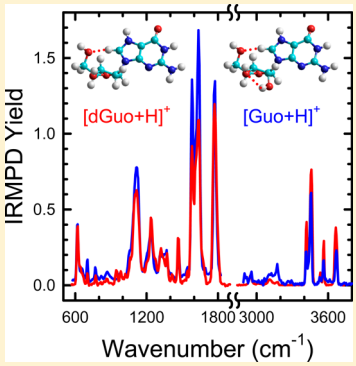

INTRODUCTION

The purine nucleobase, guanine, linked to 2′-deoxyribose or ribose via an N-glycosidic bond, forms 2′-deoxyguanosine (dGuo) or guanosine (Guo). The chemical structures of dGuo and Guo are shown in Figure 1. Both dGuo and Guo are fundamental building blocks of DNA and RNA nucleic acids. In addition to the primary roles that dGuo and Guo play in cellular biology as constituents of DNA and RNA, they are important cancer biomarkers,[1,2] and their synthetic analogues are being used as therapeutic and antiviral agents.[3,4] Among the canonical nucleobases, guanine exhibits the lowest oxidation potentials.[5] Therefore, dGuo and Guo are more susceptible to oxidative damage involving alkylating and oxidizing agents,[6,7] halogens,[8] and phenoxyl and aromatic radicals[9] than other nucleosides. 8-Hydroxy-2′-deoxyguanosine (8OHdGuo) is the most direct and frequently occurring form of oxidative damage of dGuo.[10] The N7 and O6 atoms of guanine readily interact with mono- and bivalent metal cations.[11,12] Guanine also possesses the special ability to form self-assembled tetrameric species (G-quartets) via Hoogsteen base pairing of the two hydrogen-bond donor (N1−H and N2−H) and two hydrogen-bond acceptor (O6 and N7) moieties. When G-quartets stack on top of one another, they form a G-quadruplex.[13,14] The structures of G-quadruplexes have been studied extensively because of the many G-rich and biologically significant genome regions including the immunoglobulin switch regions,[15] gene promoter regions,[16] interrupted sequences associated with human diseases,[17] and the end of chromosomes (telomeres).[18]

In addition to these important characteristics of guanine, its orientation relative to the sugar and the sugar configuration in dGuo and Guo are also crucial. For example, the sugar puckering changes from C2′-endo to C3′-endo in the transition

Received: August 7, 2014
Revised: October 31, 2014
Published: November 25, 2014

   dx.doi.org/10.1021/jp508019a | J. Phys. Chem. B 2014, 118, 14774−14784

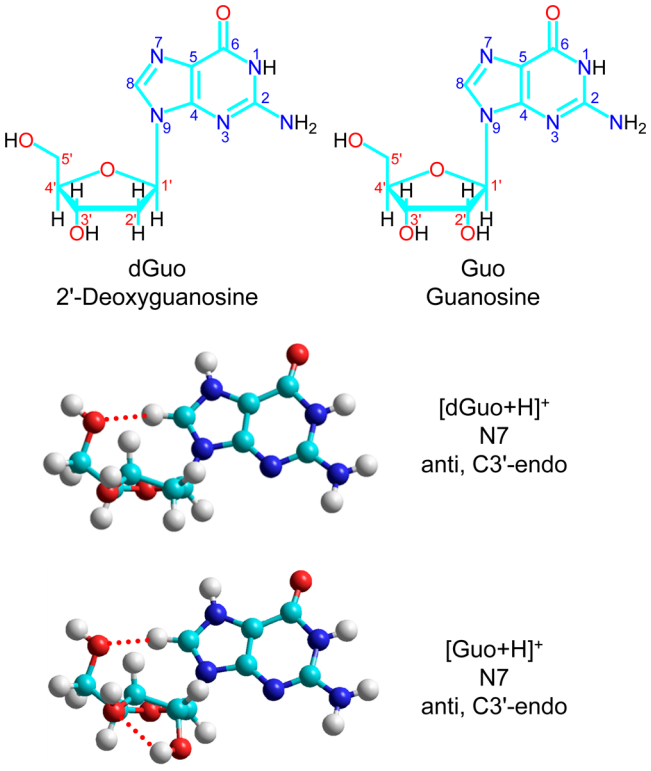

Figure 1. Chemical structures of neutral 2′-deoxyguanosine, dGuo, and guanosine, Guo. The numbering of the nucleobase and sugar is also shown. Ground-state structures of $[dGuo+H]^+$ and $[Guo+H]^+$ predicted at the B3LYP/6-311+G(2d,2p)//B3LYP/6-311+G(d,p) and MP2(full)/6-311+G(2d,2p)//B3LYP/6-311+G(d,p) levels of theory. The site of protonation, nucleobase orientation, and sugar puckering are also indicated for each protonated nucleoside.

from the B-form to the A-form of DNA[19] and from C2′-endo to C3′-endo puckering together with the rotation of the nucleobase from the "anti" to the "syn" conformation in the transition from the B-form to the Z-form of DNA.[20] In addition to the importance of nucleobase orientation and sugar puckering, hydrogen-bonding interactions also play a significant role in maintaining the overall structures and functions of DNA and RNA. Correct hydrogen-bonding interactions between base pairs[21−23] stabilize the overall DNA structure and ensure that the DNA double helix carries the correct genetic information. The hydrogen-bonding interactions between complementary base pairs may be altered if proton transfer reactions occur.[24−26] The 2′-hydroxyl substituents of the ribose moieties distinguish RNA from DNA and cause single-stranded RNA to adopt the A-form geometry involving C3′-endo puckering of the sugar rather than the B-form, which involves C2′-endo puckering of the sugar in DNA.[27] The 2′-hydroxyl group of RNA provides additional opportunities for hydrogen-bonding interactions within RNA molecules, thereby increasing the structural and functional complexity of RNA. The rapid progress of RNA crystallography has revealed a wide variety of base-pairing geometries, including sugar edge base-pairing, Watson−Crick edge base-pairing, and Hoogsteen edge base-pairing.[28,29] The pH also has a strong influence on the base-pairing geometries. Previous studies of DNA structures have found that $A^+{\cdot}C$, $A^+{\cdot}G$, $A^+{\cdot}A^+$, $C^+{\cdot}C$, and Hoogsteen $C^+{\cdot}G$ base pairs are all stabilized by protonation.[30−36] Because base pairing also plays an important role in mediating the overall structures of RNA, especially because the 2′-hydroxyl substituent may participate in sugar-edge base pairing, the effects of protonation on base-pairing geometries and overall structural features are of great interest.

Macromolecular DNA and RNA structures[37−59] have been extensively studied for decades. However, studies probing the structures of simple DNA and RNA nucleosides are very limited. A more comprehensive understanding of the structural features of nucleosides and how they are influenced by the local environment may help to better elucidate the overall structures of DNA and RNA. Previously, de Vries and co-workers[60] reported the first resonance-enhanced multiphoton ionization (REMPI)[61] spectra of neutral gas-phase guanosine nucleosides (guanosine, 2′-deoxyguanosine, and 3′-deoxyguanosine) generated by laser desorption/jet cooling. Their results suggest that the REMPI spectra of these neutral guanosines can be interpreted as resulting from both syn and anti conformers, each stabilized by intramolecular hydrogen bonding involving N3. Stueber and co-workers[62] reported the NMR measurement of the ^{13}C and ^{15}N chemical shift tensor principal values for guanosine dihydrate ($Guo{\cdot}2H_2O$) using the embedded ion method (EIM)[63] and quantum chemical calculations. They assigned the ^{13}C and ^{15}N chemical shift tensor orientations in the molecular frames of $Guo{\cdot}2H_2O$. The orientations and the magnitudes of the chemical shift principal values were correlated with the electronic structure.

In the current study, infrared multiple photon dissociation (IRMPD) action spectroscopy investigations using a Fourier transform ion cyclotron resonance mass spectrometer coupled to the FELIX free electron laser or an OPO laser system in conjunction with electronic structure calculations are performed to probe the structures and stabilities of the protonated forms of 2′-deoxyguansoine (dGuo) and its RNA analogue guanosine (Guo). Comparison between the measured IRMPD and calculated IR spectra reveals the resonant vibrational modes that induce photodissociation, the preferred sites of protonation, and the low-energy conformers that are accessed in the experiments. Comparison between $[dGuo+H]^+$ and $[Guo+H]^+$ provides insight into the effect of the 2′-hydroxyl substituent on the structures and relative stabilities of the low-energy conformations of these species. Comparison to results reported earlier for the neutral analogues enables the influence of the method of generation and protonation on structure to be elucidated.

EXPERIMENTAL AND COMPUTATIONAL SECTION

Mass Spectrometry and Photodissociation. IRMPD action spectra of protonated 2′-deoxyguanosine, $[dGuo+H]^+$, and its RNA analogue, protonated guanosine, $[Guo+H]^+$, were measured using a 4.7 T Fourier transform ion cyclotron resonance mass spectrometer (FT-ICR MS), which has been described in detail elsewhere.[64−66] Photodissociation is induced by the widely tunable free electron laser for infrared experiments (FELIX)[67]over the fingerprint region and an OPO/OPA laser system over the O−H, N−H, and C−H stretching regions. The nucleosides were purchased from Sigma-Aldrich. 0.5 mM dGuo or Guo and 5 mM acetic acid were dissolved in 50%:50% $MeOH/H_2O$ solutions. The solutions were delivered to a Micromass "Z-spray" electrospray ionization (ESI) source at a flow rate between 2.5 and 8.5 μL/min. Ions emanating from the spray were accumulated in an rf hexapole ion trap for several seconds prior to pulsed extraction through a quadrupole deflector. The ions were transferred into the FT-ICR MS via a 1 m long rf octopole ion

dx.doi.org/10.1021/jp508019a | J. Phys. Chem. B 2014, 118, 14774−14784

guide. Ion capturing was affected by electrostatic switching of the dc bias of the octopole to avoid collisional heating of the ions.[65] The ions were stored in the ICR cell to cool to room temperature by radiative emission. Typically, FELIX produces high-energy (50−100 mJ) macropulses of 1 ns spaced micropulses for a duration of about 5−10 μs. The protonated nucleosides were isolated using stored waveform inverse Fourier transform (SWIFT) techniques and irradiated for 2.5−3 s corresponding to interaction with 12−15 macropulses, respectively, from the free electron laser to induce IR photodissociation over the wavelength range between ∼18.0 μm (∼550 cm^{-1}) and ∼5.2 μm (∼1920 cm^{-1}). In addition, a benchtop optical parametric oscillator/amplifier (OPO/OPA) laser system that generates radiation in the hydrogen stretching region, at pulse energies of up to 17 mJ/pulse of 6 ns duration at 10 Hz for 4−8 s, corresponding to interaction with 40−80 pulses over the wavelength range from ∼3.6 μm (∼2800 cm^{-1}) to ∼2.6 μm (∼3800 cm^{-1}) was also used to provide complementary spectral information.

Computational Details. The chemical structures of neutral dGuo and Guo are shown in Figure 1. The nucleobase, guanine, is depicted in the anti orientation relative to the glycosidic bond in both nucleosides. The three most favorable protonation sites of $[dGuo+H]^+$ and $[Guo+H]^+$ were investigated in detail: N3, O6, and N7. Candidate structures for the neutral and each protonated form of each nucleoside were generated by simulated annealing using HyperChem software[68] with the Amber force field. Structures of interest underwent 300 cycles of simulated annealing, where each cycle involved 0.3 ps of thermal heating from 0 to 1000 K, the simulation temperature. The neutral or protonated nucleoside was then allowed to sample conformational space at 1000 K for 0.2 ps. The system was then gradually cooled down to 0 K over a period of 0.3 ps. The resulting structure was then optimized to a local minimum using the Amber force field. A molecular mechanics calculation was performed every 0.001 ps in each cycle, and a snapshot of the lowest energy structure at the end of each cycle was saved and used to initiate the subsequent cycle. Thirty candidate structures for each neutral and protonated nucleoside for each site of protonation were chosen for high level quantum chemical calculations based on the relative stabilities predicted by the simulated annealing process and their initial structural features, comprehensively including the various combinations of the favorable sites of protonation (N7, O6, and N3), sugar puckering (C2′-endo and C3′-endo), and nucleobase orientation (syn and anti). Geometry optimizations, frequency analyses, and single point energy calculations of all candidate structures were carried out using the Gaussian 09 suite of programs.[69] All candidate structures were first optimized at the B3LYP/6-31G(d) level of theory to facilitate convergence of the geometry optimization. The structures were reoptimized using the 6-311+G(d,p) basis set to improve the description of the hydrogen-bonding interactions that stabilize these systems. Linear IR spectra based on frequency analyses of the B3LYP/6-311+G(d,p) structures were computed from the resonant vibration frequencies and Raman intensities. Single point energies were calculated at the B3LYP and MP2 levels of theory using the 6-311+G(2d,2p) basis set to determine the relative stabilities of the low-energy conformers. Zero-point energy (ZPE) and thermal corrections to 298 K were included using vibrational frequencies calculated at the B3LYP/6-311+G(d,p) level of theory and scaled by a factor of 0.98 for the FELIX region and 0.957 for the OPO region. Before comparison to the experimental IRMPD spectra, the calculated vibrational frequencies are broadened using a 20 cm^{-1} fwhm Gaussion line shape.

RESULTS

IRMPD Action Spectroscopy. In both the FELIX and OPO regions, the only dissociation pathway observed for $[dGuo+H]^+$ and $[Guo+H]^+$ involves cleavage of the N-glycosidic bond, producing protonated guanine, $[Gua+H]^+$, as the ionic product detected. The IRMPD yield was determined for each protonated nucleoside, $[Nuo+H]^+$ = $[dGuo+H]^+$ or $[Guo+H]^+$, from its intensity, and the intensity of the $[Gua+H]^+$ product ion, after laser irradiation at each frequency as shown in eq 1:

$$\text{IRMPD yield} = I_{[Gua+H]^+}/(I_{[Gua+H]^+} + I_{[Nuo+H]^+}) \quad (1)$$

The IRMPD yield was normalized linearly with laser power to correct for changes in the laser power as a function of photon energy, i.e., the wavelength of the FEL or OPO lasers. IRMPD action spectra were obtained for $[dGuo+H]^+$ and $[Guo+H]^+$ over the ranges extending from ∼550 to 1900 cm^{-1} and ∼2800 to 3800 cm^{-1} and are shown in Figure 2. The IRMPD spectra of $[dGuo+H]^+$ and $[Guo+H]^+$ exhibit highly parallel spectral features in both regions. The influence of the 2′-hydroxyl substituent is seen in the relative intensities of the measured IR bands. In the FELIX region above ∼1500 cm^{-1}, $[Guo+H]^+$ exhibits higher IRMPD yield than $[dGuo+H]^+$, whereas in the OPO region above ∼3400 cm^{-1}, $[dGuo+H]^+$ produces higher IRMPD yield than $[Guo+H]^+$.

Theoretical Results. The most stable conformers of $[dGuo+H]^+$ and $[Guo+H]^+$ calculated at the B3LYP/6-311+G(2d,2p)//B3LYP/6-311+G(d,p) and MP2-(full)/6-311+G(2d,2p)//B3LYP/6-311+G(d,p) levels of theory are shown in Figure 1. Both B3LYP and MP2 predict essentially the same ground-state structures for $[dGuo+H]^+$

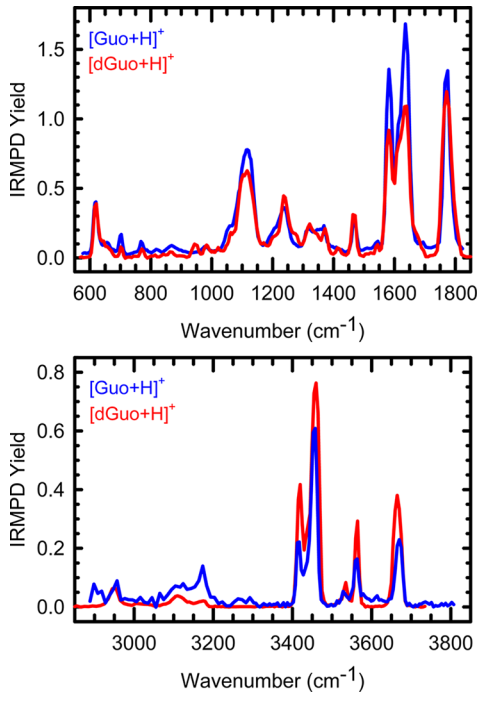

Figure 2. Infrared multiple photon dissociation (IRMPD) action spectra of $[dGuo+H]^+$ and $[Guo+H]^+$ in the FELIX and OPO regions.

dx.doi.org/10.1021/jp508019a | J. Phys. Chem. B 2014, 118, 14774−14784

and $[Guo+H]^+$. N7 is the most favorable protonation site for both $[dGuo+H]^+$ and $[Guo+H]^+$. In the ground conformers, guanine is in the anti orientation relative to the glycosidic bond and the sugar is in a C3′-endo configuration. The 2′-hydroxyl substituent does not exert a significant influence on the conformational features of the ground conformer of $[Guo+H]^+$ as compared to $[dGuo+H]^+$. The intramolecular hydrogen-bonding interaction between the 2′- and 3′-hydroxyl substituents of $[Guo+H]^+$ induces a slight change in the orientation of the 3′-hydroxyl substituent versus that of $[dGuo+H]^+$ where this interaction is absent. The slight contraction of the glycosidic bond, C1′−N9, from 1.508 Å in $[dGuo+H]^+$ to 1.498 Å in $[Guo+H]^+$, suggests that the 2′-hydroxyl substituent leads to an increase in the stability of the glycosidic bond. The hydrogen-bonding interaction between the 2′- and 3′-hydroxyl substituents of $[Guo+H]^+$ induces a small shift in the orientation of the nucleobase relative to the sugar that leads to a lengthening of the H8···O5′ noncanonical hydrogen bond from 2.075 Å in $[dGuo+H]^+$ to 2.117 Å for $[Guo+H]^+$, but has almost no effect on the orientation of the nucleobase about the glycosidic bond as the ∠C4N9C1′C2′ dihedral angle changes by only 0.2° (84.6° vs 84.8° for $[dGuo+H]^+$ vs $[Guo+H]^+$). The hydrogen-bonding interaction between the 2′- and 3′-hydroxyl substituents does not alter the sugar puckering as the ∠C1′C2′C3′C4′ dihedral angles of $[dGuo+H]^+$ and $[Guo+H]^+$ are both 31.0°. However, this hydrogen-bonding interaction does slightly influence the orientation of the 5′-hydroxymethyl substituent as the ∠O5′C5′C4′O1′ dihedral angle changes from −62.6° for $[dGuo+H]^+$ to −62.9° for $[Guo+H]^+$.

Table 1 lists the relative enthalpies and Gibbs free energies at 0 and 298 K of the low-energy conformers of $[dGuo+H]^+$ and $[Guo+H]^+$ for the various favorable protonation sites. The low-energy conformers of $[dGuo+H]^+$ and $[Guo+H]^+$ protonated at N7, O6, and N3 and their relative free energies at 298 K are shown in Figures S1 and S2 of the Supporting Information. The relative stabilities of the low-energy conformers of both $[dGuo+H]^+$ and $[Guo+H]^+$ are strongly dependent on the site of protonation. As discussed above, the ground conformers of $[dGuo+H]^+$ and $[Guo+H]^+$ are protonated at N7, whereas the most stable conformers of these species protonated at O6 and N3 are >35 and >40 kJ/mol higher in free energy, respectively. The low-energy conformers chosen for display in Figures S1 and S2 are primarily chosen based on their relative stabilities, but also include all possible combinations of the favorable protonation sites, nucleobase orientations, and sugar configurations. For the most favorable site of protonation, N7, the low-energy conformers favor the anti nucleobase orientation. Therefore, the anti conformers with C2′-endo or C3′-endo sugar puckering are included. The N7 protonated syn nucleobase conformers prefer C2′-endo sugar puckering. The O6 and N3 protonated conformers chosen here exhibit both anti and syn orientations of the nucleobase with their preferred sugar puckering. Because the 2′-hydroxyl substituent increases the opportunities for hydrogen-bonding interactions with the nucleobase, and multiple favorable orientations of the 2′- and 3′-hydroxyl substituents are available, a greater number of low-energy conformers of $[Guo+H]^+$ are found and shown here. A detailed description of the low-energy conformers shown in Figures S1 and S2 is given in the Supporting Information.

N7 Protonation. Both $[dGuo+H]^+$ and $[Guo+H]^+$ exhibit a preference for C3′-endo sugar puckering and an anti orientation of the nucleobase. Based on the relative stabilities of the low-energy conformers of $[Guo+H]^+$ with the nucleobase in the anti orientation, **N7A**, **N7B**, **N7C**, **N7D**, **N7E**, and **N7G**, it can be seen that C3′-endo sugar puckering leads to the 2′- and 3′-hydroxyl groups preferentially pointing up and away from the nucleobase, whereas C2′-endo sugar puckering results in both hydroxyl groups preferentially pointing down and away from the nucleobase. The anti nucleobase conformers are >15 kJ/mol more favorable than the syn nucleobase conformers. In the **N7D** conformer of $[dGuo+H]^+$ and the **N7F** conformer of $[Guo+H]^+$, the hydrogen-bonding interactions between the nucleobase and the 5′-hydroxyl substituent are expected to be more stabilizing than the noncanonical hydrogen-bonding interaction in the ground conformers. However, the accompanying conformational changes, i.e., rotation of the 5′-hydroxyl substituent and the orientation of the nucleobase about the glycosidic bond, destabilize both conformers by >15 kJ/mol.

Table 1. Relative Enthalpies and Free Energies at 0 and 298 K in kJ/mol of the Stable Low-Energy Conformers of $[dGuo+H]^+$ and $[Guo+H]^+$ [a]

		B3LYP			MP2(full)		
species	conformer	ΔH_0	ΔH_{298}	ΔG_{298}	ΔH_0	ΔH_{298}	ΔG_{298}
$[dGuo+H]^+$	**N7A**	**0.0**	**0.0**	**0.0**	**0.0**	**0.0**	**0.0**
	N7B	13.7	13.6	14.0	11.6	11.5	11.9
	N7C	20.1	20.4	16.6	21.2	21.4	17.7
	N7D	19.8	18.4	22.3	10.8	9.4	13.2
	N7E	32.4	34.1	27.3	30.8	32.5	25.7
	O6A	39.6	39.8	39.0	38.1	38.3	37.5
	N3A	50.3	49.8	52.4	38.9	38.3	40.9
	O6B	51.9	50.7	53.8	43.9	42.7	45.8
	N3B	93.6	95.5	90.1	90.1	91.9	86.5
$[Guo+H]^+$	**N7A**	**0.0**	**0.0**	**0.0**	**0.0**	**0.0**	**0.0**
	N7B	0.9	1.2	0.3	2.1	2.3	1.4
	N7C	3.6	3.9	3.4	2.6	2.9	2.4
	N7D	5.4	5.5	5.6	5.6	5.7	5.8
	N7E	8.7	8.4	7.5	3.7	3.5	2.6
	N7F	12.8	11.3	15.3	6.2	4.7	8.7
	N7G	17.7	17.9	15.4	18.8	19.0	16.5
	N7H	24.9	25.8	21.1	26.0	26.8	22.1
	O6A	36.2	36.8	35.0	36.4	36.9	35.2
	N3A	39.4	39.3	41.2	38.4	38.3	40.1
	O6B	46.5	45.5	48.4	40.7	39.7	42.6
	O6C	53.0	53.3	51.0	48.6	48.4	46.5
	N3B	51.6	51.6	51.3	42.3	42.3	42.0
	N3C	82.3	83.9	77.8	80.5	82.2	76.0

[a] Single point energy calculations using the B3LYP/6-311+G(d,p) optimized structures are performed at the B3LYP/6-311+G(2d,2p) and MP2(full)/6-311+G(2d,2p) levels of theory and include ZPE and thermal corrections.

O6 and N3 Protonation. O6 and N3 protonated conformers of both $[dGuo+H]^+$ and $[Guo+H]^+$ are found to be much less stable than N7 protonated conformers. Based on the relative stabilities of the O6 and N3 protonated conformers of both $[dGuo+H]^+$ and $[Guo+H]^+$, O6 protonation prefers an anti orientation of the nucleobase with C2′-endo sugar puckering, whereas N3 protonation prefers a syn orientation of the nucleobase with C3′-endo sugar puckering.

Comparison of the Low-Energy Conformers of $[dGuo+H]^+$ and $[Guo+H]^+$. The low-energy conformers of $[dGuo+H]^+$ and $[Guo+H]^+$ shown in Figures S1 and S2 exhibit highly parallel conformational features. The 2′-hydroxyl

dx.doi.org/10.1021/jp508019a | J. Phys. Chem. B 2014, 118, 14774−14784

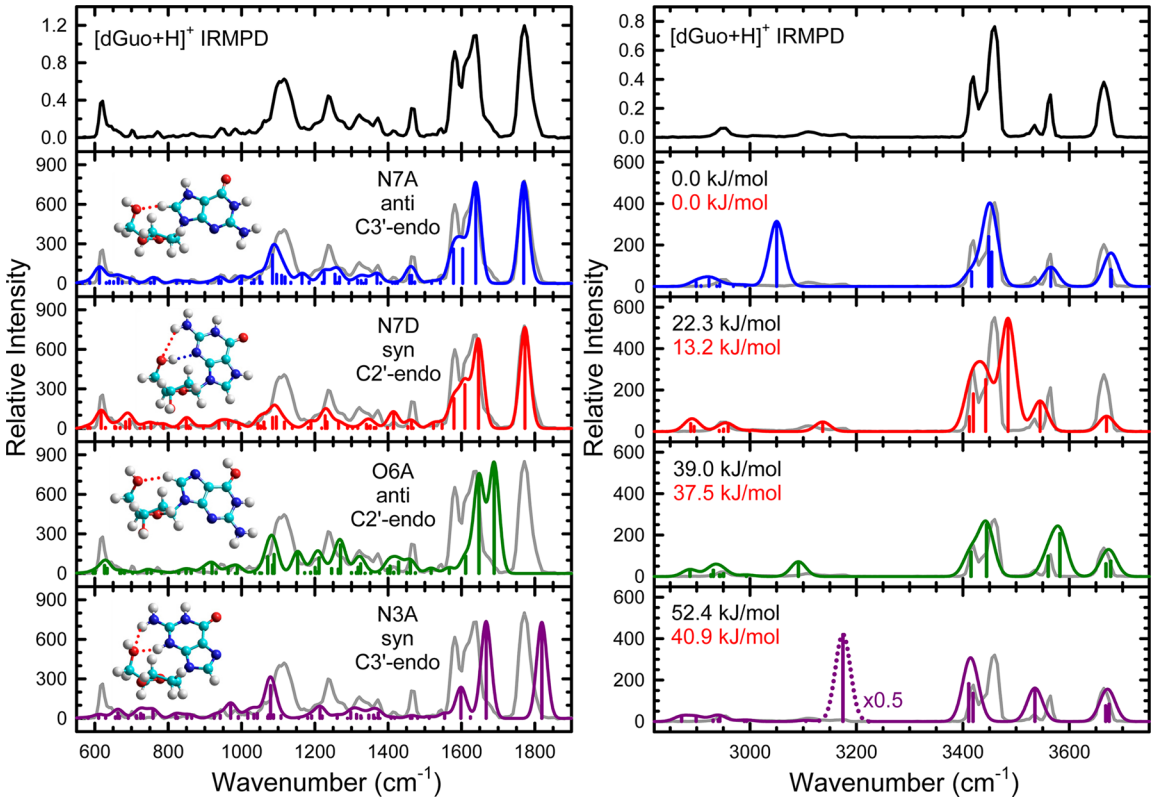

Figure 3. Comparison of the measured IRMPD action spectrum of $[dGuo+H]^+$ with the theoretical linear IR spectra for the ground-state and representative stable low-energy conformers of $[dGuo+H]^+$ and the corresponding optimized structures calculated at the B3LYP/6-311+G(d,p) level of theory. Also shown are the B3LYP/6-311+G(2d,2p) (shown in black) and MP2(full)/6-311+G(2d,2p) (shown in red) relative Gibbs free energies at 298 K. The site of protonation, nucleobase orientation, and sugar puckering are also indicated for each conformer. To facilitate comparison of the measured and computed spectra, the IRMPD spectrum is overlaid (in gray) with each computed spectrum and scaled to match the intensity of the most intense feature in each region.

substituent enables a hydrogen-bonding interaction between the 2′- and 3′-hydroxyl substituents, which may take on several favorable orientations, leading to additional stable low-energy conformers for $[Guo+H]^+$, such as the **N7C** and **N7D** conformers. The 2′-hydroxyl substituent also increases the opportunities for hydrogen bonding to the nucleobase, such as in the **N7E**, **O6C**, and **N3B** conformers of $[Guo+H]^+$. The stable low-energy conformers protonated at O6 and N3 of $[dGuo+H]^+$ and $[Guo+H]^+$ also exhibit very parallel conformational features: the **O6A**, **N3A**, and **O6B** conformers of both $[dGuo+H]^+$ and $[Guo+H]^+$ as well as the **N3B** and **N3C** conformers of $[dGuo+H]^+$ and $[Guo+H]^+$, respectively. Similar to the ground **N7A** conformers of $[dGuo+H]^+$ and $[Guo+H]^+$, these pairs of low-energy conformers share highly parallel nucleobase orientations and sugar puckering, such that the 2′-hydroxyl substituent only slightly alters the orientation of the 3′-hydroxyl substituent via the hydrogen-bonding interaction between them.

DISCUSSION

Comparison of Experimental IRMPD and Theoretical IR Spectra of $[dGuo+H]^+$. The experimental IRMPD and theoretical IR spectra of the ground and representative low-energy conformers for each favorable protonation site, **N7A**, **N7D**, **O6A**, and **N3A** of $[dGuo+H]^+$ in the FELIX and OPO regions are compared in Figure 3. In the FELIX region, the calculated IR spectra of **N7A** and **N7D** exhibit good agreement with the measured IRMPD spectrum. The change in the nucleobase orientation (anti vs syn) and the sugar puckering (C3′-endo vs C2′-endo) do not significantly change the dominant calculated IR features. In contrast, the calculated IR spectra of **O6A** and **N3A** exhibit large discrepancies as compared to the measured IRMPD spectrum in the FELIX region, especially above ∼1500 cm^{-1}, indicating that the site of protonation exerts a significant influence on the IR features in this region. In the OPO region, only the calculated IR spectrum of **N7A** exhibits good agreement with the measured IRMPD spectrum, whereas the calculated IR spectra of the other three conformers show obvious discrepancies. The calculated band at ∼3545 cm^{-1} of **N7D** is red-shifted relative to the measured band at ∼3565 cm^{-1}, whereas the band predicted at ∼3485 cm^{-1} is blue-shifted relative to the measured band at ∼3460 cm^{-1}. The calculated band at ∼3580 cm^{-1} of **O6A** is blue-shifted relative to the measured band at ∼3565 cm^{-1}, whereas the band predicted at ∼3445 cm^{-1} is red-shifted relative to the measured band at ∼3460 cm^{-1}. The IR bands at ∼3535 and ∼3415 cm^{-1} calculated for **N3A** are both red-shifted relative to the measured bands at ∼3565 and ∼3460 cm^{-1}, respectively. Therefore, the ground **N7A** conformer is accessed in the experiments, whereas the **N7D** conformer with the nucleobase in the syn orientation is not. The O6 and N3 protonated conformers are also not populated in the experiments. It is worth noting that very weak C−H stretches occur in the OPO region below ∼3300 cm^{-1}. These very weak IR features are generally not very useful for diagnostic purposes. In addition, because of the noncanonical C8H···O5′ hydrogen bond, the

dx.doi.org/10.1021/jp508019a | J. Phys. Chem. B 2014, 118, 14774−14784

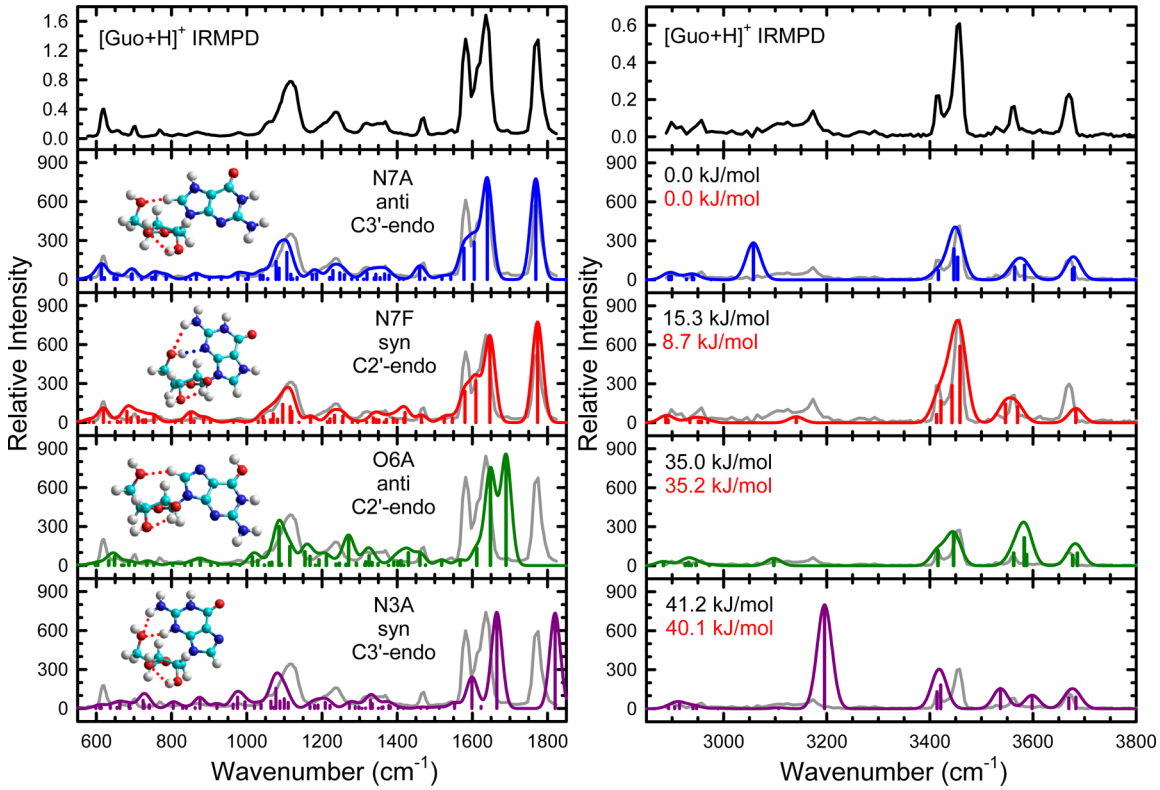

Figure 4. Comparison of the measured IRMPD action spectrum of $[Guo+H]^+$ with the theoretical linear IR spectra for the ground-state and representative stable low-energy conformers of $[Guo+H]^+$ and the corresponding optimized structures calculated at the B3LYP/6-311+G(d,p) level of theory. Also shown are the B3LYP/6-311+G(2d,2p) (shown in black) and MP2(full)/6-311+G(2d,2p) (shown in red) relative Gibbs free energies at 298 K. The site of protonation, nucleobase orientation, and sugar puckering are also indicated for each conformer. To facilitate comparison of the measured and computed spectra, the IRMPD spectrum is overlaid (in gray) with each computed spectrum and scaled to match the intensity of the most intense feature in each region.

calculated band at ~3100 cm^{-1} of **N7A**, representing the harmonic C8−H stretch, is not a good descriptor for this anharmonic mode, and thus is also not diagnostically useful.

Figure S3 compares the experimental IRMPD and theoretical IR spectra of the **N7B**, **N7C**, **N7E**, **O6B**, and **N3B** conformers of $[dGuo+H]^+$ in the FELIX and OPO regions. In the FELIX region, the calculated IR spectrum of **N7B** exhibits good agreement with the measured IR spectrum and is highly parallel to that of **N7A** (Figure 3). The calculated IR band at ~1060 cm^{-1} of **N7C** and ~1040 cm^{-1} of **N7E** would broaden the measured IR band at ~1120 cm^{-1} if these two conformers were accessed in the experiments. Rotation of the 5′-hydroxymethyl substituent away from the nucleobase shifts the associated IR bands of **N7C** and **N7E** to ~1050 cm^{-1}, providing a poor match to the measured band at ~1120 cm^{-1}. The calculated IR spectra of **O6B** and **N3B** exhibit large discrepancies with the measured IRMPD spectrum in the FELIX region. In the OPO region, only the calculated IR spectrum of **N7B** exhibits good agreement with the measured IRMPD spectrum, whereas the calculated IR spectra of the other four conformers all exhibit obvious spectra differences. Therefore, in addition to the ground-state **N7A** conformer, only the **N7B** conformer is accessed in the experiments.

In summary, comparison of the calculated IR featuress to those observed experimentally in the FELIX and OPO regions indicates that only the two most stable N7 protonated conformers, **N7A** and **N7B**, are accessed in the experiments. Based on the computed relative stabilities of these conformers, the experiments should be predominantly populated by the ground **N7A** conformer. These comparisons also enable vibrational assignments of the measured IRMPD spectral features to be made. In the FELIX region, the strong and sharp IR absorption measured at ~1770 cm^{-1} arises from C═O stretching. The broader band at ~1640 cm^{-1} with a sharp shoulder at ~1580 cm^{-1} primarily reflects NH_2 scissoring and C4═C5 stretching coupled with N1−H in-plane bending, respectively. The small sharp peak observed at ~1470 cm^{-1} arises from C2′H_2 scissoring. The sharp but moderate absorption at ~1240 cm^{-1} represents N7−H in-plane bending, whereas the broader IR band at ~1120 cm^{-1} is associated with sugar ring stretching. In the OPO region, the moderate IR absorption measured at ~3665 cm^{-1} reflects coupled O3′−H and O5′−H stretching. The weak but sharp IR band measured at ~3565 cm^{-1} is associated with NH_2 asymmetric stretching, whereas the strong IR absorption observed at ~3460 cm^{-1} reflects strong coupled NH_2 symmetric and N1−H stretching. The very small peak at ~3535 cm^{-1} is not predicted for the **N7A** or **N7B** conformers, suggesting that this feature is the first overtone of the intense C═O stretch observed at ~1770 cm^{-1}.

Comparison of Experimental IRMPD and Theoretical IR Spectra of $[Guo+H]^+$. The experimental IRMPD and theoretical IR spectra of the ground and representative low-energy conformers for each favorable protonation site, **N7A**, **N7F**, **O6A**, and **N3A** of $[Guo+H]^+$ in the FELIX and OPO regions are compared in Figure 4. In the FELIX region, the calculated IR spectrum of the ground **N7A** conformer reproduces the experimental IRMPD spectrum quite well. Although guanine is rotated into the syn orientation with a

dx.doi.org/10.1021/jp508019a | J. Phys. Chem. B 2014, 118, 14774−14784

hydrogen bond between N3 and O5′H in the **N7F** conformer, the calculated IR signatures above ~1500 cm^{-1} do not differ appreciably from those of **N7A**. Below ~1500 cm^{-1}, the calculated IR features of **N7F** also exhibit reasonably good agreement with the measured IRMPD spectrum. As found for $[dGuo+H]^+$, the FELIX region is not as informative for differentiating nucleobase orientation, sugar puckering, and the 2′-, 3′-, and 5′-hydroxyl orientations. The calculated IR spectra of **O6A** and **N3A**, however, exhibit large discrepancies as compared to the measured IRMPD spectrum, especially above ~1500 cm^{-1}, again indicating that the site of protonation is readily determined based on the IR features in this region. Therefore, O6 and N3 protonated conformers are not accessed in the experiments. As discussed above, the C−H stretches predicted below ~3300 cm^{-1} in the OPO region generally do not reproduce the measured C−H stretching features very well. The IR features observed above ~3300 cm^{-1} are diagnostic and enable the conformers present in the experiments to be determined. As suggested for $[dGuo+H]^+$, the small IR feature observed at ~3535 cm^{-1} is likely the first overtone of the carbonyl stretch at ~1770 cm^{-1}. The calculated IR spectrum of **N7A** exhibits good agreement with the measured IRMPD spectrum in the OPO region. The calculated IR bands at ~3685 cm^{-1} of **N7F** and **O6A** are blue-shifted relative to the measured band at ~3670 cm^{-1}. The IR features of **N7F** predicted at ~3570 and ~3545 cm^{-1} would broaden the IR band measured at ~3560 cm^{-1}. Also, the IR features of **N7F** predicted at ~3460 and ~3440 cm^{-1} would lead to broadening of the sharp IR band observed at ~3450 cm^{-1}. The IR band predicted at ~3575 cm^{-1} for **O6A** is blue-shifted relative to the measured band at ~3560 cm^{-1}. The IR bands predicted at ~3440 cm^{-1} for **O6A** and at ~3410 cm^{-1} for **N3A** are red-shifted relative to the measured band at ~3450 cm^{-1}. The calculated IR bands at ~3600 and ~3535 cm^{-1} of **N3A** are blue-shifted and red-shifted, respectively, relative to the measured band at ~3560 cm^{-1}. Therefore, among these conformers only the ground-state **N7A** conformer is accessed in the experiments.

Figure S4 compares the experimental IRMPD and theoretical IR spectra of the **N7B**, **N7C**, **N7D**, **N7E**, and **N7G** conformers of $[Guo+H]^+$ in the FELIX and OPO regions. In the FELIX region, the calculated IR spectra of **N7B**, **N7C**, **N7D**, and **N7E** are highly parallel to the calculated IR spectrum of **N7A** (Figure 4), and all agree reasonably well with the measured IRMPD spectrum. Therefore, the changes of the sugar configuration and the orientations of 2′- and 3′-hydroxyl substituents of these four conformers cannot be distinguished from the calculated IR spectra in the FELIX region. Because the 5′-hydroxymethyl substituent is rotated away the nucleobase in the **N7G** conformer of $[Guo+H]^+$, the moderate IR band predicted at ~1050 cm^{-1} for this conformer, which is not predicted for the **N7A**, **N7B**, **N7C**, **N7D**, and **N7E** conformers, eliminates **N7G** as this band is not observed in the measured IRMPD spectrum. In the OPO region, the calculated IR spectrum of **N7B**, parallel to the calculated IR spectrum of **N7A** (Figure 4), exhibits good agreement with the measured IRMPD spectrum. The calculated IR spectra of **N7C**, **N7D**, and **N7E** also provide a good match to the measured IRMPD spectrum in the OPO region. The weak IR bands predicted at ~3605 cm^{-1} for **N7C**, at ~3615 cm^{-1} for **N7D**, and at ~3620 cm^{-1} for **N7E**, which are not predicted for **N7A** and **N7B**, may contribute to the small and broad IR band observed at ~3610 cm^{-1}. The IR band predicted at ~3690 cm^{-1} for **N7G** is blue-shifted relative to the measured band at ~3670 cm^{-1}, and the IR feature predicted at ~3585 cm^{-1} is not observed in the measured IRMPD spectrum, and therefore this conformer is not present in the experiments. Therefore, along with the ground-state **N7A** conformer, the **N7B**, **N7C**, **N7D**, and **N7E** conformers are also accessed in the experiments in minor populations.

Figure S5 compares the experimental IRMPD and theoretical IR spectra of the **N7H**, **O6B**, **O6C**, **N3B**, and **N3C** conformers of $[Guo+H]^+$ in the FELIX and OPO regions. In the FELIX region, the change in the orientation of 5′-hydroxymethyl substituent of **N7H** leads to a band predicted at ~1050 cm^{-1}, which if this conformer were present would broaden the band observed at ~1120 cm^{-1}. In addition, the band predicted at ~960 cm^{-1} is not observed in the measured IRMPD spectrum. Thus, **N7H** is not accessed in the experiments. The calculated IR spectra of **O6B**, **O6C**, **N3B**, and **N3C** show large discrepancies with the measured IRMPD spectrum in the FELIX region. In the OPO region, the calculated IR spectrum of **N7H** exhibits good agreement with the measured IRMPD spectrum, but its presence is already eliminated based on the comparison in the FELIX region. The calculated IR spectra of **O6B** and **O6C** again exhibit very large differences from the measured IRMPD spectrum in the OPO region. The calculated bands at ~3680 cm^{-1} for **N3B** and at ~3685 cm^{-1} for **N3C** are blue-shifted relative to the measured band at ~3670 cm^{-1}. The calculated bands at ~3535 and ~3440 cm^{-1} for **N3B** and at ~3545 and ~3430 cm^{-1} for **N3C** are red-shifted relative to the measured bands at ~3560 and ~3450 cm^{-1}, respectively. Therefore, the **N7H**, **O6B**, **O6C**, **N3B**, and **N3C** conformers are not accessed in the experiments.

In summary, comparison of the calculated IR features to those observed experimentally in the FELIX and OPO regions indicate that the N7 protonated low-energy conformers **N7A**, **N7B**, **N7C**, **N7D**, and **N7E** are accessed in the experiments and allows peak assignments to be made. In the FELIX region, the strong sharp IR absorption at ~1770 cm^{-1} represents the carbonyl stretch. The strong IRMPD band observed at ~1635 cm^{-1} arises from NH_2 scissoring, whereas the shoulder to the red at ~1580 cm^{-1} arises from nucleobase stretches. The small sharp peak observed at ~1470 cm^{-1} reflects C2′H_2 scissoring. The sharp moderate absorption at ~1240 cm^{-1} represents N7−H in-plane bending, whereas the broader IR band at ~1120 cm^{-1} arises from sugar ring stretching. In the OPO region, the measured IRMPD band at ~3670 cm^{-1} reflects coupling of the 3′- and 5′-hydroxyl stretches. The IR feature measured at ~3560 cm^{-1} is associated with coupling of the 2′-hydroxyl and asymmetric NH_2 stretches. The small IR feature appearing at ~3535 cm^{-1} is the first overtone of the carbonyl stretch at ~1770 cm^{-1}. The sharp IR absorption at ~3450 cm^{-1} represents N7−H stretch coupled with symmetric NH_2 stretches, whereas the shoulder to the red at ~3410 cm^{-1} arises from N1−H stretching.

Comparison of Experimental IRMPD and Maxwell−Boltzmann Weighted Theoretical IR Spectra. On the basis of comparisons between the measured IRMPD and calculated IR spectra for the low-energy conformers of $[dGuo+H]^+$ and $[Guo+H]^+$, we conclude that the **N7A** and **N7B** conformers of $[dGuo+H]^+$ and the **N7A**, **N7B**, **N7C**, **N7D**, and **N7E** conformers of $[Guo+H]^+$ are accessed in the experiments. However, the relative stabilities of these low-energy conformers differ somewhat depending upon whether they are determined at the B3LYP or MP2 level of theory. In an attempt to determine which theory provides a better description of the relative stabilities of the low-energy conformations of

dx.doi.org/10.1021/jp508019a | J. Phys. Chem. B 2014, 118, 14774−14784

$[dGuo+H]^+$ and $[Guo+H]^+$, we compare the measured IRMPD spectra of these species to the linear IR spectra calculated based on a statistically weighted average of the relevant conformers based on their relative Maxwell−Boltzmann populations at room temperature determined using the B3LYP and MP2 levels of theory. Results for $[dGuo+H]^+$ are shown in Figure S8, whereas results for $[Guo+H]^+$ are shown in Figure S9. As can be seen in the figures, the Maxwell−Boltzmann weighted spectra calculated at the B3LYP and MP2 levels of theory both exhibit very good agreement with the measured IRMPD spectra. However, the agreement does not noticeably improve as compared to that found for comparison to the ground conformers, suggesting that the populations of the excited conformers in the experiments must be small. In addition, the results are strikingly similar for B3LYP and MP2 theory such that no firm conclusion regarding the relative accuracies of these methods can be made based on these comparisons. Comparisons among the computed low-energy conformers (i.e., **N7D**, **N3A**, and **O6B** conformers of $[dGuo+H]^+$ and the **N7E**, **N7F**, **O6B**, **O6C**, and **N3B** conformers of $[Guo+H]^+$) suggest that MP2 exhibits a bias for conformations that involve canonical hydrogen-bonding interactions and find that these interactions are more stabilizing than found using B3LYP.

Effects of Protonation of the Structures of dGuo and Guo. In order to elucidate the effects of protonation on the structures of dGuo and Guo, we also performed calculations for neutral dGuo and Guo as described in the Computational Details section. The low-energy conformers of dGuo and Guo determined and their relative free energies at 298 K are shown in Figures S6 and S7 of the Supporting Information. The relative enthalpies and Gibbs free energies at 0 and 298 K of the low-energy conformers of dGuo and Guo are also listed in Table S1. Both dGuo and Guo prefer guanine in a syn orientation with 5′-hydroxyl moiety rotated toward the N3 atom of guanine and C2′-endo sugar puckering. B3LYP predicts the keto forms as the ground conformers, whereas MP2 predicts enol forms associated with an N1−O6 tautomeric shift to be the ground conformers. The ground conformers of dGuo and Guo differ markedly from those of $[dGuo+H]^+$ and $[Guo+H]^+$, which adopt an anti orientation of the nucleobase and C3′-endo sugar puckering. The **N7D** and **N7F** conformers of $[dGuo+H]^+$ and $[Guo+H]^+$, respectively, which lie >15 kJ/mol above the ground **N7A** conformers, exhibit a marked resemblance to the B3LYP ground conformers of neutral dGuo and Guo (except of course for the presence of the excess proton). Therefore, theory indicates that protonation markedly alters the preferred nucleobase orientation, sugar puckering, and the relative stabilities of the low-energy conformations of dGuo and Guo.

Comparison to Other Gas-Phase Techniques. de Vries and co-workers[70] previously examined the neutral forms of 9-ethylguanine, guanosine, and 2′-deoxyguanosine in the mid-IR region, 500−2000 cm^{-1}, using UV−IR double resonance techniques and theoretical calculations. The most stable conformers calculated for both Guo and dGuo in their study using the RIMP2/cc-pVDZ level of theory exhibit C2′-endo puckering of the ribose and 2′-deoxyribose sugars, and syn nucleobase orientations that are stabilized by a hydrogen-bonding interaction between the N3 nitrogen atom of the nucleobase and the 5′-hydroxyl hydrogen atom of the sugar moiety, which are consistent with the B3LYP ground **neuA** conformers of dGuo and Guo calculated here. The next most stable conformers deVries and co-workers found for both Guo and dGuo are the enol forms of the ground conformers, which have undergone an N1−O6 tautomeric shift, and are consistent with the MP2 ground **neuB** conformers of dGuo and Guo calculated here. However, comparison of the IR−UV ion-dip spectrum of Guo and dGuo to the theoretical IR spectra calculated using both the RI-MP2/ccpVDZ and RI-DFT-D (TSSP) levels of theory suggests that the slightly higher energy enol tautomers were accessed in their experiments due to the absence of a sharp carbonyl stretch at ∼1700−1725 cm^{-1}. This is markedly different from the results observed in the current study in which a strong carbonyl stretch is present in the IRMPD action spectra of $[dGuo+H]^+$ and $[Guo+H]^+$ at ∼1770 cm^{-1}, indicating that the ground canonical keto tautomers of the protonated nucleosides were accessed in our experiments. Guo and dGuo were introduced into the gas phase via laser desorption in the IR−UV experiments, whereas in the current work, electrospray ionization (ESI) was employed here to generate the protonated species. Thus, the tautomeric conformations accessed are sensitive to both the method of generation and the state of protonation. In addition, in principle, the vibrational modes of the ribose from the IR−UV experiments can be used to compare to the modes observed in the current study in an attempt to assign different conformations, C2′-endo vs C3′-endo, of the deoxyribose and ribose moieties. However, the vibrational modes below 1350 cm^{-1} in the IRMPD action spectra of $[dGuo+H]^+$ and $[Guo+H]^+$ are significantly broadened as compared to the IR−UV ion-dip spectra of dGuo and Guo, and the coupling of the sugar and nucleobase vibrational modes makes such a comparison very difficult. Therefore, such comparisons were not pursued, as they would probably not yield very useful information.

Comparison to Condensed-Phase Techniques. NMR spectroscopy[71,72] and X-ray crystallography[73,74] are useful techniques for characterizing the structures of molecules and, in particular, nucleic acids in the condensed phases. However, studies of the simple nucleosides in the condensed phase are rare. Sychrovsky and co-workers[75] studied the dependence of six *J* NMR spin−spin coupling constants on the geometries of dGuo and Guo by comprehensive computational calculations and compared their results to values measured for larger related nucleic acids. They also modeled the effect of various base-pairing interactions on the *J* coupling magnitudes. They found that Guo adopts a conformation consistent with the RNA Watson−Crick/sugar edge (WC/SE) class of base pairs. The structure of Guo involved in WC/SE base pairs is similar to that of the **neuD** conformer of Guo calculated here. The 2′-hydroxyl substituent enables a hydrogen-bonding interaction with N3 of guanine, which is not feasible for dGuo, again indicating that the 2′-hydroxyl moiety provides additional opportunities for hydrogen-bonding interactions, and therefore may alter conventional base pair patterns or may even create new base-pairing interactions.

CONCLUSIONS

The IRMPD action spectra of protonated 2′-deoxyguanosine, $[dGuo+H]^+$, and protonated guanosine, $[Guo+H]^+$, in the regions of 550−1900 and 2800−3800 cm^{-1} were measured and compared with linear IR spectra predicted for the stable low-energy conformers of these species determined at the B3LYP/6-311+G(d,p) level of theory. Comparisons between the measured IRMPD and calculated IR spectra in these two regions complement and support each other, enabling the

dx.doi.org/10.1021/jp508019a | J. Phys. Chem. B 2014, 118, 14774−14784

conformer(s) accessed in the experiments to be determined. The site of protonation is easily distinguished in the calculated IR spectra in both regions. N7 is the most favorable protonation site for both $[dGuo+H]^+$ and $[Guo+H]^+$, followed by O6 and then N3, consistent with the relative site-specific proton affinities of guanine computed by Russo and co-workers.[76] The calculated IR spectra of N7 protonated low-energy conformers of $[dGuo+H]^+$ and $[Guo+H]^+$ in the FELIX region are highly parallel and challenging to distinguish. Comparison between experiment and theory of the N7 protonated conformers in the OPO region provides additional valuable information, facilitating conformer assignments. Based on these comparisons, N7 protonated conformers **N7A** and **N7B** of $[dGuo+H]^+$ and **N7A**, **N7B**, **N7C**, **N7D**, and **N7E** of $[Guo+H]^+$ are accessed in the experiments, whereas obvious discrepancies between the measured and computed spectra rule out the presence of O6 and N3 protonated conformers. In all of the N7 protonated conformers of $[dGuo+H]^+$ and $[Guo+H]^+$ accessed in the experiments, guanine is in the anti orientation and the conformers are stabilized by a weak noncanonical hydrogen bond between C8−H and O5′ except for **N7E** of $[Guo+H]^+$, where the anti orientation of guanine is maintained by the dual N3···O2′−H···O3′−H hydrogen-bonding interactions. The hydrogen-bonding interaction between the 2′- and 3′-hydroxyl substituents of $[Guo+H]^+$ influences IVR such that the IRMPD yield of $[Guo+H]^+$ above ∼1500 cm^{-1}, the nucleobase IR signature region, exceeds that of $[dGuo+H]^+$. In contrast, the greater flexibility of the free 3′-hydroxyl substituent of $[dGuo+H]^+$ versus the hydrogen-bonded 3′-hydroxyl of $[Guo+H]^+$ leads to greater IRMPD yield for $[dGuo+H]^+$ than $[Guo+H]^+$ above ∼3300 cm^{-1}. The ionic species produced by the ESI source are consistent among the protonated DNA vs RNA nucleosides such that only N7 protonated, anti oriented, and the canonical keto forms of the guanine residue of $[dGuo+H]^+$ and $[Guo+H]^+$ are accessed in the experiments.

■ ASSOCIATED CONTENT

Supporting Information

Complete citation for ref 69; a detailed description of and figures showing the structures of the B3LYP/6-311+G(d,p) low-energy conformers of $[dGuo+H]^+$ and $[Guo+H]^+$ and their relative Gibbs free energies at 298 K calculated at the B3LYP/6-311+G(2d,2p) and MP2(full)/6-311+G(2d,2p) levels of theory; comparisons of the measured IRMPD spectra and calculated linear IR spectra in the FELIX and OPO regions of select low-energy conformers of $[dGuo+H]^+$ and $[Guo+H]^+$; structures of the B3LYP/6-311+G(d,p) low-energy conformers of neutral dGuo and Guo and their relative Gibbs free energies at 298 K calculated at the B3LYP/6-311+G(2d,2p) and MP2(full)/6-311+G(2d,2p) levels of theory; comparisons of the measured IRMPD spectra and Maxwell−Boltzmann weighted IR spectra calculated for the low-energy conformers of $[dGuo+H]^+$ and $[Guo+H]^+$ accessed in the experiments and based on energetics calculated at the B3LYP and MP2 levels of theory. This material is available free of charge via the Internet at http://pubs.acs.org.

■ AUTHOR INFORMATION

Corresponding Author

*E-mail mrodgers@chem.wayne.edu (M.T.R.).

Notes

The authors declare no competing financial interest.

■ ACKNOWLEDGMENTS

Financial support of this work was provided by the National Science Foundation, Grants PIRE-0730072 and CHE-1409420. R.R.W. also gratefully acknowledges support from a Thomas C. Rumble Graduate Fellowship at Wayne State University. We also thank WSU C&IT for the computational resources and support. This work is part of the research program of FOM, which is financially supported by the Nederlandse Organisatie voor Wetenschappeklijk Onderzoek (NWO). The skillful assistance of the FELIX staff is gratefully acknowledged.

■ REFERENCES

(1) Waalkes, T. P.; Abeloff, M. D.; Ettinger, D. S.; Woo, K. B.; Gehrke, C. W.; Kuo, K. C.; Borek, E. Modified Ribonucleosides As Biological Markers for Patients with Small Cell-Carcinoma of the Lung. *Eur. J. Cancer Clin. Oncol.* **1982**, *18*, 1267−1274.

(2) Mitchell, E. P.; Evans, L.; Schultz, P.; Madsen, R.; Yarbro, J. W.; Gehrke, C. W.; Kuo, K. Modified Nucleosides in Human Serum. *J. Chromatogr.* **1992**, *581*, 31−40.

(3) Perigaud, C.; Gosselin, G.; Imbach, J. L. Stereospecific Synthesis of Chiral Acyclic Analogs of Guanosine. *Bioorg. Med. Chem. Lett.* **1992**, *2*, 677−680.

(4) Perigaud, C.; Gosselin, G.; Imbach, J. L. Nucleoside Analogs As Chemotherapeutic-Agents − A Review. *Nucleosides Nucleotides* **1992**, *11*, 903−945.

(5) Bjelland, S.; Seeberg, E. Mutagenicity, Toxicity and Repair of DNA Base Damage Induced by Oxidation. *Mutat. Res.* **2003**, *531*, 37−80.

(6) Burrows, C. J.; Muller, G. Oxidative Nucleobase Modifications Leading to Strand Scission. *Chem. Rev.* **1998**, *98*, 1109−1151.

(7) Wiseman, H.; Halliwell, B. Damage to DNA by Reactive Oxygen and Nitrogen Species: Role in Inflammatory Disease and Progression to Cancer. *Biochem. J.* **1996**, *313*, 17−29.

(8) Masuda, M.; Suzuki, T.; Friesen, M. D.; Ravanat, J. L.; Cadet, J.; Pignatelli, B.; Nishino, H.; Ohshima, H. Chlorination of Guanosine and Other Nucleosides by Hypochlorous Acid and Myeloperoxidase of Activated Human Neutrophils − Catalysis by Nicotine and Trimethylamine. *J. Biol. Chem.* **2001**, *276*, 40486−40496.

(9) Liu, J.-A.; Petzold, C. J.; Ramirez-Arizmendi, L. E.; Perez, J.; Kenttamaa, H. Phenyl Radicals React with Dinucleoside Phosphates by Addition to Purine Bases and H-Atom Abstraction From a Sugar Moiety. *J. Am. Chem. Soc.* **2005**, *127*, 12758−12759.

(10) Serrano, J.; Palmeira, C. M.; Wallace, K. B.; Kuehl, D. W. Determination of 8-Hydroxydeoxyguanosine in Biological Tissue by Liquid Chromatography/Electrospray Ionization-Mass Spectrometry/Mass Spectrometry. *Rapid Commun. Mass Spectrom.* **1996**, *10*, 1789−1791.

(11) Burda, J. V.; Sponer, J.; Hobza, P. *Ab Initio* Study of the Interaction of Guanine and Adenine with Various Mono- and Bivalent Metal Cations (Li^+, Na^+, K^+, Rb^+, Cs^+; Cu^+, Ag^+, Au^+; Mg^{2+}, Ca^{2+}, Sr^{2+}, Ba^{2+}, Zn^{2+}, Cd^{2+} and Hg^{2+}). *J. Phys. Chem.* **1996**, *100*, 7250−7255.

(12) Lippert, B. Multiplicity of Metal Ion Binding Patterns to Nucleobases. *Coord. Chem. Rev.* **2000**, *200*, 487−516.

(13) Neidle, S.; Read, M. A. G-Quadruplexes as Therapeutic Targets. *Biopolymers* **2001**, *56*, 195−208.

(14) Lyonnais, S.; Hounsou, C.; Teulade-Fichou, M.; Jeusset, J.; Cam, E. L.; Mirambeau, G. G-Quartets Assembly within a G-Rich DNA Flap. A Possible Event at the Center of the HIV-1 Genome. *Nucleic Acids Res.* **2002**, *30*, 5276−5283.

(15) Sen, D.; Gilbert, W. Formation of Parallel 4-Stranded Complexes by Guanine-Rich Motifs in DNA and Its Implications for Meiosis. *Nature* **1988**, *334*, 364−366.

(16) Evans, T.; Schon, E.; Gora-Maslak, G.; Patterson, J.; Efstratiadis, A. S1-Hypersensitive Sites in Eukaryotic Promoter Regions. *Nucleic Acids Res.* **1984**, *12*, 8043−8058.
(17) Sarig, G. Purification and Characterization of qTBP42 a New Single-Stranded and Quadruplex Telomeric DNA-Binding Protein from Rat Hepatocytes. *J. Biol. Chem.* **1997**, *272*, 4474−4482.
(18) Blackburn, E. H. Telomeres − No End in Sight. *Cell* **1994**, *77*, 621−623.
(19) van Dam, L.; Ouwerkerk, N.; Brinkmann, A.; Raap, J.; Levitt, M. H. Solid-State NMR Determination of Sugar Ring Pucker in C-13-Labeled 2′-Deoxynucleosides. *Biophys. J.* **2002**, *83*, 2835−2844.
(20) Rich, A.; Nordheim, A.; Wang, A. H. The Chemistry and Biology of Left-Handed Z-DNA. *J. Annu. Rev. Biochem.* **1984**, *53*, 791−846.
(21) Nir, E.; Janzen, C.; Imhof, P.; Kleinermanns, K.; de Veries, M. S. Pairing of the Nucleobases Guanine and Cytosine in the Gas Phase Studied by IR-UV Double-Resonance Spectroscopy and *ab initio* Calculation. *Phys. Chem. Chem. Phys.* **2002**, *4*, 732−739.
(22) Nir, E.; Janzen, C.; Imhof, P.; Kleinermanns, K.; de Veries, M. S. Pairing of the Nucleobase Guanine Studied by IR-UV Double-Resonance Spectroscopy and *Ab Initio* Calculation. *Phys. Chem. Chem. Phys.* **2002**, *4*, 740−750.
(23) Hanus, M.; Ryjacek, F.; Kabelac, M.; Kubar, T.; Bogdan, T. V.; Trygubenko, S. A.; Hobza, P. Correlated *Ab Initio* Study of Nucleic Acid Bases and Their Tautomers in the Gas Phase, in a Microhydrated Environment and in Aqueous Solution. Guanine: Surprising Stabilization of Rare Tautomers in Aqueous Solution. *J. Am. Chem. Soc.* **2003**, *125*, 7678−7688.
(24) Guallar, V.; Douhal, A.; Moreno, M.; Lluch, J. M. DNA Mutations Induced by Proton and Charge Transfer in the Low-lying Excited Singlet Electronic States of the DNA Base Pairs: A Theoretical Insight. *J. Phys. Chem. A* **1999**, *103*, 6251−6256.
(25) Zoete, V.; Meuwly, M. Double Proton Transfer in the Isolated and DNA-Embedded Guanine-Cytosine Base Pair. *J. Chem. Phys.* **2004**, *121*, 4377−4388.
(26) Li, X.; Cai, Z.; Sevilla, M. D. Investigation of Proton Transfer within DNA Base Pair Anion and Cation Radicals by Density Functional Theory (DFT). *J. Phys. Chem. B* **2001**, *105*, 10115−10123.
(27) Salazar, M.; Fedoroff, O. Y.; Miller, J. M.; Ribeiro, N. S.; Reid, B. R. The DNA Strand in DNA•RNA Hybrid Duplexes is Neither B-form nor A-form in Solution. *Biochemistry* **1993**, *32*, 4207−4215.
(28) Batey, R. T.; Rambo, R. P.; Doudna, J. A. Tertiary Motifs in RNA Structure and Folding. *Angew. Chem., Int. Ed.* **1999**, *38*, 2326−2343.
(29) Westhof, E.; Fritsch, V. RNA Folding: Beyond Watson−Crick Pairs. *Struct. Fold Des.* **2000**, *8*, R55−R65.
(30) Wang, C.; Gao, H.; Gaffney, B. L.; Jones, R. A. Nitrogen-15-Labeled Oligodeoxynucleotides. 3. Protonation of the Adenine N1 in the A•C and A•G Mispairs of the Duplexes {d[CG(^{15}N^{1})-AGAATTCCCG]}^{2} and {d[CGGGAATTC(^{15}N^{1})ACG]}^{2}. *J. Am. Chem. Soc.* **1991**, *113*, 5486−5488.
(31) Leroy, J. L.; Gehring, K.; Kettani, A.; Gueron, M. Acid Multimers of Oligodeoxycytidine Strands: Stoichiometry, Base-Pair Characterization, and Proton Exchange Properties. *Biochemistry* **1993**, *32*, 6019−6031.
(32) Moser, H. E.; Dervan, P. B. Sequence-Specific Cleavage of Double Helical DNA by Triple Helix Formation. *Science* **1987**, *238*, 645−650.
(33) Rajagopal, P.; Feigon, J. Triple-Strand Formation in the Homopurine: Homopyrimidine DNA Oligonucleotides d(G•A)$_4$ and d(T•C)$_4$. *Nature* **1989**, *239*, 637−639.
(34) de los Santos, C.; Rosen, M.; Patel, D. NMR Studies of DNA $(R^+)_n$•$(Y^-)_n$•$(Y^+)_n$ Triple Helices in Solution: Imino and Amino Proton Markers of T•A•T and C•G•C$^+$ Base-Triple Formation. *Biochemistry* **1989**, *28*, 7282−7290.
(35) Xodo, L. E.; Manzini, G.; Quadrifoglio, F.; van der Marel, G. A.; van Boom, J. H. Effect of 5-Methylcytosine on the Stability of Triple-Stranded DNA-A Thermodynamic Study. *Nucleic Acids Res.* **1991**, *19*, 5625−5631.
(36) Singleton, S. F.; Dervan, P. B. Influence of pH on the Equilibrium Association Constants for Oligodeoxyribonucleotide-Directed Triple Helix Formation at Single DNA Sites. *Biochemistry* **1992**, *31*, 10995−11003.
(37) McPherson, A.; Jurnak, F.; Wang, A.; Kolpal, F.; Rich, A.; Molineux, I.; Fitzgerald, P. The Structure of A DNA Unwinding Protein and Its Complexes With Oligodeoxynucleotides by X-Ray-Diffraction. *Biophys. J.* **1980**, *32*, 155−173.
(38) Delamaza, L. M.; Carter, B. J. Molecular Structure of Adeno-Associated Virus Variant DNA. *J. Biol. Chem.* **1980**, *255*, 3194−3203.
(39) Guo, Q.; Lu, M.; Churchill, M. E. A.; Tullius, T. D.; Kallenbach, N. R. Asymmetric Structure of a Three-Arm DNA Junction. *Biochemistry* **1990**, *29*, 10927−10934.
(40) Pina, B.; Truss, M.; Ohlenbusch, H.; Postma, J.; Beato, M. DNA Rotational Positioning in a Regulatory Nucleosome is Determined By Base Sequence − An Algorithm to Model the Preferred Superhelix. *Nucleic Acids Res.* **1990**, *18*, 6981−6987.
(41) Vanmeervelt, L.; Moore, M. H.; Lin, P. K. T.; Brown, D. M.; Kennard, O. Molecular and Crystal-Structure of d(CGCGmo^{4}CG) − N^4 − Methoxycytosine. Guanine Base-Pairs in Z-DNA. *J. Mol. Biol.* **1990**, *216*, 773−781.
(42) Florian, J.; Leszczynski, J. Theoretical Investigation of the Molecular-Structure of the Pi-Kappa DNA-Base Pair. *J. Biomol. Struct. Dyn.* **1995**, *12*, 1055−1062.
(43) Santamaria, R.; Quirozgutierrez, A.; Juarez, C. Structures and Energetic Properties of B-DNA Nucleotides. *J. Mol. Struct.: THEOCHEM* **1995**, *357*, 161−170.
(44) Triolo, A.; Arcamone, F. M.; Raffaelli, A.; Salvadori, P. Non-Covalent Complexes Between DNA-Binding Drugs and Double-Stranded Deoxyoligonucleotides: A Study by Ionspray Mass Spectrometry. *J. Mass Spectrom.* **1997**, *32*, 1186−1194.
(45) Wang, Z.; Wan, K. X.; Ramanathan, R.; Taylor, J. S.; Gross, M. L. Structure and Fragmentation Mechanism of Isomeric T-Rich Oligodeoxynucleotides: A Comparison of Four Tandem Mass Spectrometric Methods. *J. Am. Soc. Mass Spectrom.* **1998**, *9*, 683−691.
(46) Cheatham, T. E.; Srinivasan, J.; Case, D. A.; Kollman, P. A. Molecular Dynamics and Continuum Solvent Studies of the Stability of polyG-polyC and polyA-polyT DNA Duplexes in Solution. *J. Biomol. Struct. Dyn.* **1998**, *16*, 265−280.
(47) Kurnikov, I. V.; Tong, G. S. M.; Madrid, M.; Beratan, D. N. Hole Size and Energetics in Double Helical DNA: Competition Between Quantum Delocalization and Solvation Localization. *J. Phys. Chem. B* **2002**, *106*, 7−10.
(48) Rueda, M.; Kalko, S. G.; Luque, F. J.; Orozco, M. The Structure and Dynamics of DNA in the Gas Phase. *J. Am. Chem. Soc.* **2003**, *125*, 8007−8014.
(49) Guo, X. H.; Bruist, M. F.; Davis, D. L.; Bentzley, C. M. Secondary Structural Characterization of Oligonucleotide Strands Using Electrospray Ionization Mass Spectrometry. *Nucleic Acids Res.* **2005**, *33*, 3659−3666.
(50) Balthasart, F.; Plavec, J.; Gabelica, V. Ammonium Ion Binding to DNA G-Quadruplexes: Do Electrospray Mass Spectra Faithfully Reflect the Solution-Phase Species? *J. Am. Soc. Mass Spectrom.* **2013**, *24*, 1−8.
(51) Jaeger, J. A.; Turner, D. H.; Zuker, M. Predicting Optimal and Suboptimal Secondary Structure for RNA. *Methods Enzymol.* **1990**, *183*, 281−306.
(52) Estes, P. A.; Cooke, N. E.; Liebhaber, S. A. A Native RNA Secondary Structure Controls Alternative Splice-Site Selection and Generates 2 Human Growth-Hormone Isoforms. *J. Biol. Chem.* **1992**, *267*, 14902−14908.
(53) Gutell, R. R.; Power, A.; Hertz, G. Z.; Putz, E. J.; Stormo, G. D. Identifying Constraints on the Higher-Order Structure of RNA − Continued Development and Application of Comparative Sequence-Analysis Methods. *Nucleic Acids Res.* **1992**, *20*, 5785−5795.
(54) Davis, D. R. Stabilization of RNA Stacking by Pseudouridine. *Nucleic Acids Res.* **1995**, *23*, 5020−5026.

(55) Jones, S.; Daley, D. T. A.; Luscombe, N. M.; Berman, H. M.; Thornton, J. M. Protein-RNA Interactions: A Structural Analysis. *Nucleic Acids Res.* **2001**, *29*, 943−954.
(56) Gooch, B. D.; Beal, P. A. Recognition of Duplex RNA by Helix-Threading Peptides. *J. Am. Chem. Soc.* **2004**, *126*, 10603−10610.
(57) Koculi, E.; Hyeon, C.; Thirumalai, D.; Woodson, S. A. Charge Density of Divalent Metal Cations Determines RNA Stability. *J. Am. Chem. Soc.* **2007**, *129*, 2676−2682.
(58) Zhang, A. Y. Q.; Bugaut, A.; Balasubramanian, S. A Sequence-Independent Analysis of the Loop Length Dependence of Intramolecular RNA G-Quadruplex Stability and Topology. *Biochemistry* **2011**, *50*, 7251−7258.
(59) Philips, A.; Milanowska, K.; Lach, G.; Boniecki, M.; Rother, K.; Bujnicki, J. M. MetalionRNA: Computational Predictor of Metal-Binding Sites in RNA Structures. *Bioinformatics* **2012**, *28*, 198−205.
(60) Nir, E.; Imhof, P.; Kleinermanns, K.; de Vries, M. S. REMPI Spectroscopy of Laser Desorbed Guanosines. *J. Am. Chem. Soc.* **2000**, *122*, 8091−8092.
(61) Nir, E.; Grace, L.; Brauer, B.; de Vries, M. S. REMPI Spectroscopy of Jet-Cooled Guanine. *J. Am. Chem. Soc.* **1999**, *121*, 4896−4897.
(62) Stueber, D.; Grant, D. M. C-13 and N-15 Chemical Shift Tensors in Adenosine, Guanosine Dihydrate, 2′-Deoxythymidine, and Cytidine. *J. Am. Chem. Soc.* **2002**, *124*, 10539−10551.
(63) Stueber, D.; Guenneau, F. N.; Grant, D. M. The Calculation of C-13 Chemical Shielding Tensors in Ionic Compounds Utilizing Point Charge Arrays Obtained From Ewald Lattice Sums. *J. Chem. Phys.* **2001**, *114*, 9236−9243.
(64) Valle, J. J.; Eyler, J. R.; Oomens, J.; Moore, D. T.; van der Meer, A. F. G.; von Heldon, G.; Meijer, G.; Hendrickson, C. L.; Marshall, A. G.; Blakney, G. T. Free Electron Laser-Fourier Transform Ion Cyclotron Resonance Mass Spectrometry Facility for Obtaining Infrared Multiphoton Dissociation Spectra of Gaseous Ions. *Rev. Sci. Instrum.* **2005**, *76*, 023103−1−023103−7.
(65) Polfer, N. C.; Oomens, J.; Moore, D. T.; von Helden, G.; Meijer, G.; Dunbar, R. C. Infrared Spectroscopy of Phenylalanine Ag(I) and Zn(II) Complexes in the Gas Phase. *J. Am. Chem. Soc.* **2006**, *128*, 517−525.
(66) Polfer, N. C.; Oomens, J. Reaction Products in Mass Spectrometry Elucidated with Infrared Spectroscopy. *Phys. Chem. Chem. Phys.* **2007**, *9*, 3804−3817.
(67) Oepts, D.; van der Meer, A. F. G.; van Amersfoort, P. W. The Free-Electron-Laser User Facility FELIX. *Infrared Phys. Techn.* **1995**, *36*, 297−308.
(68) HyperChem Computational Chemistry Software Package, Version 5.0; Hypercube, Inc., Gainsville, FL, 1997.
(69) Frisch, M. J.; Trucks, G. W.; Schlegel, H. B.; Scuseria, G. E.; Robb, M. A.; Cheeseman, J. R.; Scalmani, G.; Barone, V.; Mennucci, B.; Petersson, G. A.; et al. *Gaussian 09, Revision C.01*; Gaussian, Inc.: Wallingford, CT, 2009. See Supporting Information for full reference.
(70) Abo-riziq, A.; Crews, B. O.; Compagnon, I.; Oomens, J.; Meijer, G.; von Helden, G.; Kabelac, M.; Hobza, P.; de Vries, M. S. The Mid-IR Spectra of 9-Ethyl Guanine, Guanosine, and 2′-Deoxyguanosine. *J. Phys. Chem. A* **2007**, *111*, 7529−7536.
(71) Wijmenga, S. S.; van Buuren, B. N. M. The Use of NMR Methods for Conformational Studies of Nucleic Acids. *Prog. NMR Spectrosc.* **1998**, *32*, 287−387.
(72) Flinders, J.; Dieckmann, T. NMR Spectroscopy of Ribonucleic Acids. *Prog. NMR Spectrosc.* **2006**, *48*, 137−159.
(73) Wimberly, B. T.; Brodersen, D. E.; Clemons, W. M.; Morgan-Warren, R. J.; Carter, A. P.; Vonrhein, C.; Hartsch, T.; Ramakrishnan, V. Structure of the 30S Ribosomal Subunit. *Nature* **2000**, *407*, 327−339.
(74) Schuwirth, B. S.; Borovinskaya, M. A.; Hau, C. W.; Zhang, W.; Vila-Sanjurjo, A.; Holton, J. M.; Cate, J. H. D. Structures of the Bacterial Ribosome at 3.5 Angstrom Resolution. *Science* **2005**, *310*, 827−834.
(75) Vokacova, Z.; Bickelhaupt, F. M.; Sponer, J. Y.; Sychrovsky, V. Structural Interpretation of *J* Coupling Constants in Guanosine and Deoxyguanosine: Modeling the Effects of Sugar Pucker, Backbone Conformation, and Base Pairing. *J. Phys. Chem. A* **2009**, *113*, 8379−8386.
(76) Russo, N.; Toscano, M.; Grand, A.; Jolibis, F. Protonation of Thymine, Cytosine, Adenine, and Guanine DNA Nucleic Acid Bases: Theoretical Investigation into the Framework of Density Functional Theory. *J. Comput. Chem.* **1998**, *9*, 989−1000.